metals

MDPI

Article

Corrosion Response of Co-6Ti-11V-9Cr Alloy in Acidic Chloride Solutions

Peilin Chen [1], Wenhua Li [1], Anpeng Ke [1], Pengjie Zhang [2], Bujun Ge [1], Tao Chen [3] and Xiaoru Zhuo [3,*]

[1] The Guangzhu Electric Power Co., Ltd., Zhuhai SEZ, Zhuhai 519060, China
[2] Luoyang Shuangrui Wanji Titanium Industry Co., Ltd., Luoyang 471832, China
[3] School of Materials Science and Engineering, Jiangsu University of Science and Technology, Zhenjiang 212100, China
* Correspondence: xrzhuo@just.edu.cn

Abstract

The corrosion response of a Co-6Ti-11V-9Cr superalloy was investigated in 0.05 mol/L H_2SO_4 containing 0, 0.01, 0.1 or 0.5 mol/L NaCl. Open-circuit potential (OCP), electrochemical impedance spectroscopy (EIS), potentiodynamic polarisation, scanning electron microscopy (SEM) and electrochemical noise (EN) analysis were combined to determine how chloride concentration affects passive-film stability and localised corrosion. Increasing the NaCl concentration shifted both the OCP and corrosion potential in the negative direction. The fitted resistance of the barrier layer decreased from 4.61×10^4 to 0.39×10^4 Ω cm^2, whereas the passive current density increased from 4.58×10^{-6} to 1.78×10^{-5} A cm^{-2}. SEM and EN analyses further showed that chloride enrichment promoted local passive-film breakdown, changing the surface response from relatively uniform corrosion to localised attack and pitting. These findings provide an experimental basis for assessing Co-Ti-V-based superalloys in acidic chloride-containing service environments.

Keywords: Co-based superalloy; electrochemical impedance spectroscopy; potentiodynamic polarisation; electrochemical noise; pitting corrosion

1. Introduction

Superalloys retain structural stability under high-temperature and high-pressure conditions and typically offer high strength, corrosion resistance and oxidation resistance. They are therefore indispensable structural materials for biomedical, aerospace, energy and petrochemical applications [1–5]. These alloys are commonly based on Co, Fe or Ni. Among them, Ni-based superalloys are the most widely used. Their γ/γ' strengthening architecture gives them excellent high-temperature strength and oxidation resistance, and Ni-based alloys account for 52.7% of high-temperature components in aerospace systems [6,7]. However, Ni-based alloys remain vulnerable to corrosion-related failure in specific environments, including pipeline transport systems [8,9]. Such degradation can compromise component reliability, cause equipment failure and create safety risks. Developing next-generation structural alloys that combine high toughness with corrosion resistance is therefore a persistent challenge.

Compared with Ni-based alloys, Co-based alloys have intrinsic advantages in wear resistance and chemical corrosion resistance, particularly in sulphidising and acidic media, because of their electronic structure. They are therefore widely used as hard-facing materials [10,11]. Eliaz et al. [12] further showed that Co-based alloys can exhibit better

Check for updates

Academic Editor: Petros E. Tsakiridis

Received: 31 July 2026
Revised: 11 September 2026
Accepted: 14 September 2026
Published: 15 September 2026

Copyright: © 2026 by the authors. Licensee MDPI, Basel, Switzerland. This article is an open access article distributed under the terms and conditions of the Creative Commons Attribution (CC BY) license.

hot-corrosion resistance than Ni-based alloys in environments containing sulphur and vanadium impurities, making them attractive for stationary components in petrochemical equipment. Conventional Co-based alloys, however, lack a coherent γ' strengthening phase analogous to that in Ni-based superalloys. Their strengthening relies mainly on carbides, which limits their overall performance.

To address this limitation, increasing attention has been directed towards γ'-strengthened Co-based superalloys. In 2006, Sato et al. [13] reported a Co-Al-W superalloy strengthened by a coherent γ/γ' microstructure. The γ'-Co3(Al,W) phase closely resembles the principal strengthening phase in Ni-based superalloys and has a lattice misfit of only 0.53%, which enables effective precipitation strengthening. First-principles calculations by Yao et al. [14] also indicated that the $L1_2$ structure of γ'-Co3(Al,W) is thermodynamically stable and has a higher elastic modulus than the matrix. These findings provided an important basis for Co-Al-W alloy design and stimulated broader research on γ'-strengthened Co-based superalloys [15–17]. Within the Co-Ni-Al-W system, Bocchini et al. [18] demonstrated that partial substitution of Al and W by Ti can increase the γ' volume fraction. The same substitution can also raise the antiphase-boundary energy, thereby impeding dislocation motion and improving high-temperature yield strength.

Although Co-Al-W alloys revived interest in Co-based superalloys, the high density of W restricts their use in weight-sensitive aerospace applications. Makineni et al. [19] therefore proposed a W-free design strategy and developed Co-Al-Mo-Nb alloys in which Mo and Nb stabilise the $L1_2$ γ' phase. This design reduced alloy density while retaining high specific yield strength. Liu et al. [20] further showed that V addition can tune the γ/γ' lattice misfit to a low-misfit range, suppress γ' coarsening and improve microstructural stability. Ruan et al. [21] subsequently developed an $L1_2$-strengthened Co-Ti-V-based superalloy and compared it directly with the commercial Ni-based alloy IN-939. That alloy reproduced the anomalous yield-strength peak characteristic of Ni-based superalloys and showed comparable, or even higher, mechanical performance above 850 °C.

High-temperature mechanical performance alone is not sufficient for engineering use of Co-Ti-V-based superalloys. In petrochemical and oil-and-gas transport environments, corrosion resistance often governs service life and operational safety. Current studies of Co-Ti-V-based alloys have focused mainly on high-temperature mechanical properties [22,23], whereas corrosion studies have largely considered simpler NaCl-containing media [24]. Zhang et al. [24] reported the cavitation erosion-corrosion behaviour of a Co-6Ti-11V-9Cr superalloy in 3.5% NaCl solution and provided static electrochemical baseline data including corrosion potential and corrosion current density for this alloy under neutral chloride-rich conditions. Their work offers a valuable reference for understanding the corrosion nature of the same Co-Ti-V-Cr-based superalloy. Nonetheless, corrosion behaviour of Co-Ti-V-based superalloys in more aggressive environments, where acidity and chloride ions coexist, remains less well understood. In practical petrochemical and energy-related service environments, Co-based alloy components often encounter acidic media containing both sulphate and chloride impurities. Because aggressive anions are small, mobile and strongly destabilising under acidic conditions, they can penetrate and weaken passive films, thereby reducing corrosion protection.

Accordingly, 0.05 mol/L H_2SO_4 electrolytes with different NaCl concentrations (0, 0.01, 0.1 and 0.5 mol/L) were adopted in this work, aiming to reveal the influences of chloride ions on passive-film stability and corrosion behaviours of a Co-6Ti-11V-9Cr superalloy under acidic corrosive conditions. This acidic chloride-containing system simulates practical service environments in petrochemical and energy industries, where structural components are subjected to combined attack from H^+, sulphate and chloride ions. Keeping the concentration of H_2SO_4 unchanged, we focus on clarifying the influence of the chloride

concentration on the passive-film stability and corrosion responses of a Co-6Ti-11V-9Cr superalloy under an acidic-sulphate background. It should be noted that this experimental design cannot completely separate the individual roles of H^+, SO_4^{2-} and Cl^-. Further studies using NaCl-only solutions without H_2SO_4 will help to distinguish the independent effect of chloride ions.

2. Materials and Methods

2.1. Material Preparation

Metallic cobalt, titanium, vanadium and chromium (each 99.9% in purity) were selected as starting materials, and alloy ingots with a nominal composition of Co-6Ti-11V-9Cr were fabricated in a WK-2-type non-consumable vacuum arc-melting furnace. The chemical composition of the alloy, determined by inductively coupled plasma (ICP) analysis, is given in Table 1.

Table 1. Chemical composition of the Co-6Ti-11V-9Cr superalloy (at.%).

Co	Ti	V	Cr
Bal.	6 ± 0.02	11 ± 0.03	9 ± 0.01

2.2. Microstructural Characterisation

Selective electrochemical etching was conducted in a 1.5 L electrolytic cell containing 10 wt.% oxalic acid solution (pH = 1.2). A constant-voltage mode of 5 V DC was used. After etching, the specimens were immediately removed, ultrasonically cleaned in anhydrous ethanol for 3 min, rinsed with deionised water and dried in cold air. Microstructures were examined using a ZEISS Sigma 500 field-emission scanning electron microscope (SEM; Carl Zeiss Microscopy GmbH, Oberkochen, Germany) operated in high-resolution imaging mode at an accelerating voltage of 15 kV. Elemental distributions were obtained using an OXFORD X-MaxN 20 energy-dispersive X-ray spectroscopy detector (Oxford Instruments NanoAnalysis, Abingdon, UK). Phase composition of the alloy was analysed by an X-ray diffractometer (XRD) over a 2θ scan range of 20–90°, with a scanning rate of 4°/min.

2.3. Electrochemical Measurements

Electrochemical measurements were performed using a Gamry Reference 600+ electrochemical workstation (Gamry Instruments, Inc., Philadelphia, PA, USA) in a conventional three-electrode configuration. The working electrode had an exposed surface area of 100 mm^2. The base electrolyte used in all experiments was 0.05 mol/L H_2SO_4. The target alloy was used as the working electrode, a saturated calomel electrode (SCE) as the reference electrode and a platinum sheet as the counter electrode. Before testing, cathodic polarisation was applied at −1.2 V versus SCE for 120 s to remove the native surface oxide. OCP was then monitored for 1 h until the system reached a quasi-steady state. EIS measurements were collected at the stabilised OCP over 10^{-2} to 10^4 Hz with a 10 mV perturbation amplitude. The spectra were fitted using ZView software (version: ZView2). Potentiodynamic polarisation was conducted from −0.5 to +1.2 V versus OCP at 0.333 mV s^{-1} and was terminated when the current density reached 1 mA cm^{-2}. Each condition was measured three times to evaluate data reproducibility.

2.4. Electrochemical Noise Measurements

Before EN testing, the specimens were rinsed with deionised water, ultrasonically cleaned in anhydrous ethanol and dried with hot air. Measurements were then conducted immediately inside a Faraday shield. The cell used two nominally identical working electrodes from the same batch and an SCE reference electrode. The test media were the

four acidic chloride solutions, and the temperature was maintained at 25 ± 2 °C. EN signals were acquired using a Gamry Reference 600+ workstation. The sampling frequency was 10 Hz, the segment length was 1024 points, and the total test duration was 10 h. Data post-processing used detrending and filtering to reduce direct-current drift. Wavelet analysis and shot-noise parameters were then used to assess localised corrosion behaviour.

The corrosion media were 0.05 mol/L H_2SO_4 + x mol/L NaCl solutions, where x = 0, 0.01, 0.1 and 0.5. OCP, EIS and potentiodynamic polarisation measurements were combined with SEM observations after polarisation. EN analysis was used to further resolve localised corrosion events in the different acidic chloride solutions.

3. Results and Discussion

3.1. Phase Constitution and Microstructure

Figure 1 shows the X-ray diffraction pattern of the Co-6Ti-11V-9Cr superalloy. Figure 2 presents the etched SEM microstructure. The alloy contains a γ/γ' two-phase structure and a Co_3V phase. In the magnified γ/γ' region, grey blocky γ' precipitates are separated by γ-matrix channels.

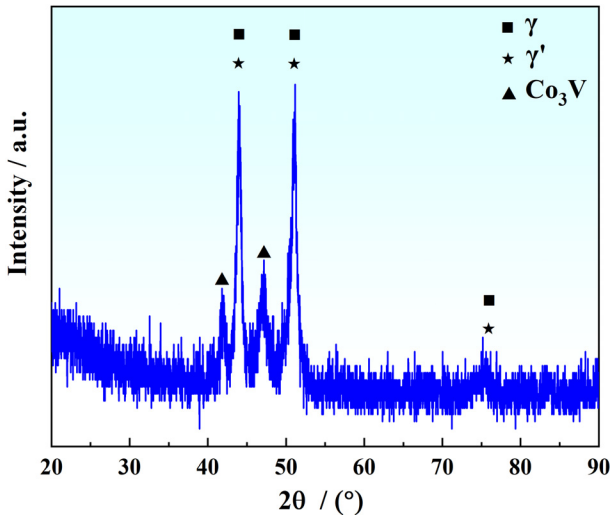


Figure 1. X-ray diffraction patterns (XRD) of the Co-6Ti-11V-9Cr superalloy. The identified phases are indexed as γ (FCC Co-based solid solution, JCPDS No. 15-0806), γ' ($L1_2$-ordered Co_3Ti phase, JCPDS No. 23-0938) and Co_3V (JCPDS No. 12-0378).

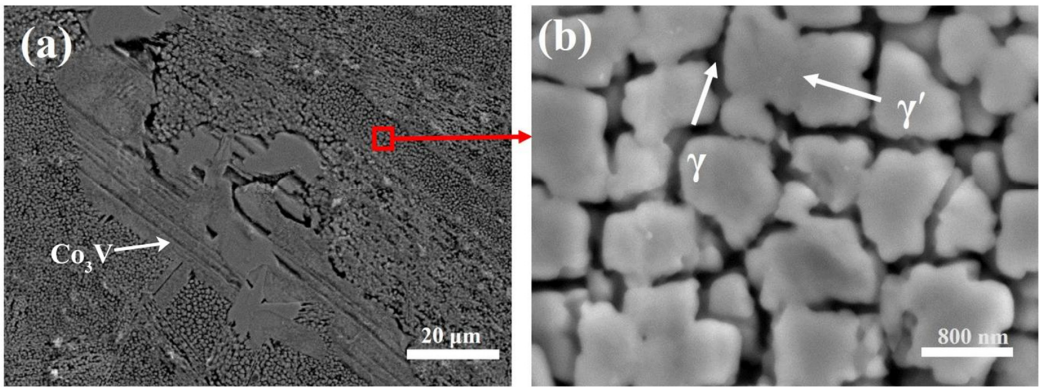


Figure 2. Microstructure of the Co-6Ti-11V-9Cr superalloy, (**a**) Co_3V and (**b**) γ and γ'.

3.2. Open-Circuit Potential

Figure 3 shows the time-dependent OCP of the Co-6Ti-11V-9Cr superalloy in the four acidic chloride solutions. In all solutions, the OCP shifted in the positive direction with

time and approached a stable value after approximately 2400 s, indicating that the passive film reached a relatively steady state. As the NaCl concentration increased, the OCP shifted negatively. This trend indicates that chloride ions destabilised the passive film, activated the alloy surface and increased the thermodynamic tendency for corrosion. The highest OCP, approximately −0.22 V versus SCE, was measured in 0.05 mol/L H_2SO_4 without added NaCl. The lowest OCP, approximately −0.30 V versus SCE, occurred in 0.05 mol/L H_2SO_4 + 0.5 mol/L NaCl. The OCP response therefore shows that the corrosion tendency increased with the chloride concentration.

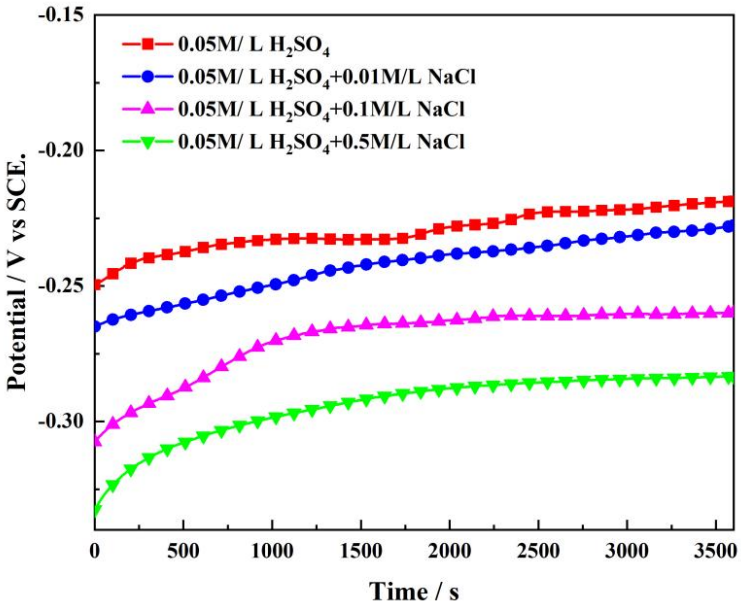


Figure 3. Open-circuit potential of the Co-6Ti-11V-9Cr alloy in the tested solutions.

3.3. Electrochemical Impedance Spectroscopy

Figure 4 shows the EIS response of the Co-6Ti-11V-9Cr alloy in the four acidic chloride solutions. The spectra had similar overall shapes, suggesting that chloride concentration did not substantially change the passive-film-controlled impedance response. In the Nyquist plots (Figure 4a), all solutions produced depressed capacitive arcs with two time constants, which can be associated with the passive film and the electrochemical double layer. As the chloride concentration increased, the arc height and diameter decreased markedly, indicating a reduction in corrosion resistance.

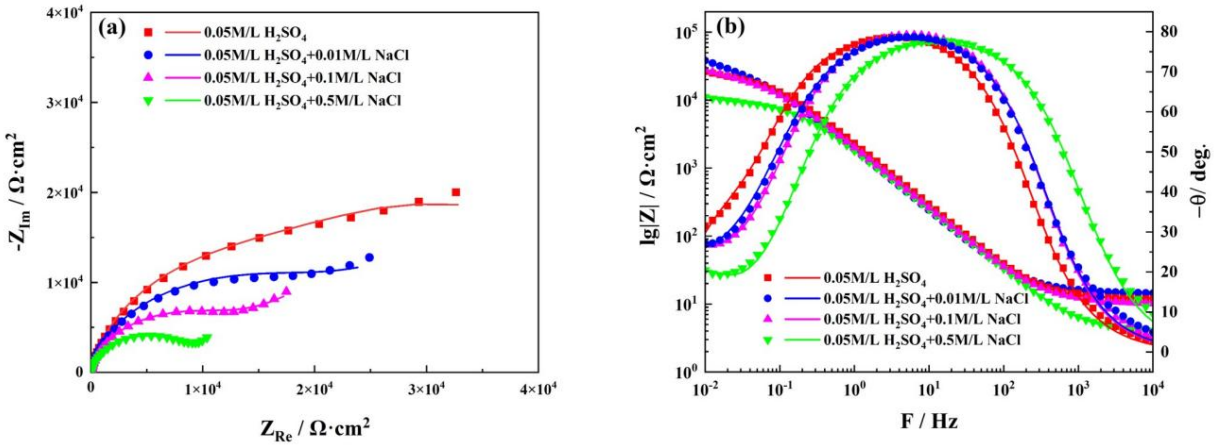


Figure 4. EIS response of the Co-6Ti-11V-9Cr alloy in the four acidic chloride solutions: (**a**) Nyquist plots and (**b**) Bode plots.

In the Bode phase plots (Figure 4b), the phase angle approached 0° near 10^4 Hz, showing that the high-frequency impedance was dominated by solution resistance. Between 10^2 and 10^{-1} Hz, the phase angle was close to −80°, consistent with a protective passive film with pseudo-capacitive behaviour. In the middle-to-low-frequency region, the impedance increased as the frequency decreased, and the slope of log | Z | versus log f approached −1. Between 0.1 and 0.01 Hz, the increase in phase angle slowed. These features indicate that corrosion was mainly controlled by charge transport through the passive film and the electrochemical double layer.

The EIS spectra were fitted using the equivalent circuit shown in Figure 5. The chi-square values were on the order of 10^{-4}, indicating acceptable fitting quality. In this circuit, R_s is the solution resistance and W represents the Warburg impedance associated with diffusion. Q denotes a constant phase element (CPE). Q_{f1} and Q_{f2} correspond to the capacitances of the porous outer layer and barrier inner layer, respectively, whereas R_{f1} and R_{f2} represent their resistances. Because the current distribution on the working electrode surface is non-ideal, the CPE impedance is expressed as

$$Z_{\mathrm{CPE}} = Q^{-1}(jw)^{-n} \tag{1}$$

where j is the imaginary unit ($j^2 = -1$), ω is the angular frequency and n is the CPE dispersion exponent.

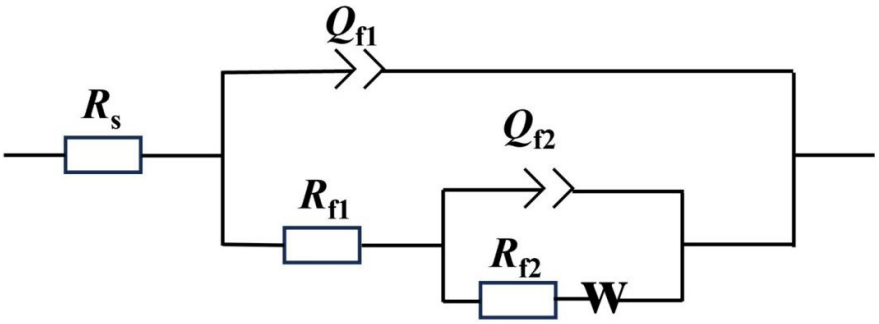


Figure 5. Equivalent circuit used to fit the EIS spectra.

The fitted electrochemical parameters were used to estimate the passive-film thickness. According to the power-law model, the film thickness can be calculated from Equations (2) and (3):

$$C_0 = Q^{\frac{1}{n}} \cdot R_p^{n(1-n)} \tag{2}$$

$$D = \frac{\varepsilon \varepsilon_0 A}{C_0} \tag{3}$$

where C_0 is the passive-film capacitance, ε is the dielectric constant (15.6), ε_0 is the vacuum permittivity (8.85×10^{-14} F cm^{-1}), A is the working-electrode area (1.83 cm^2), and D is the passive-film thickness.

The fitted EIS parameters are listed in Table 2. The n values of the Co-6Ti-11V-9Cr alloy fell between 0.5 and 1, indicating that the CPE response associated with the passive film combined Warburg-type and capacitive characteristics. For all solutions, the barrier-layer resistance R_{f2} was much higher than R_{f1}, showing that the protective effect of the passive film mainly originated from the inner barrier layer. According to previous reports on Co-Cr-based alloys, the passive film formed on this Co-6Ti-11V-9Cr alloy is tentatively considered to be mainly composed of oxides including Cr_2O_3 and CoO/Co_3O_4 [25,26]. The decrease in R_{f2} with increasing Cl^- concentration suggests that Cl^- ions can penetrate and chemically react with the oxide film, leading to the formation of soluble metal–chloride complexes and thereby thinning or destroying the barrier layer. The polarisation resistance

R_p, which reflects the resistance to corrosion damage [27], is the zero-frequency limit of the impedance and can be approximated as $R_p = R_{f1} + R_{f2}$. A higher R_p generally indicates better corrosion resistance. Here, R_p decreased progressively with an increasing NaCl concentration, showing that chloride addition made the alloy more susceptible to corrosion.

Table 2. EIS fitting parameters for the Co-6Ti-11V-9Cr alloy in the four acidic chloride solutions.

NaCl Concentration	0 mol/L	0.01 mol/L	0.1 mol/L	0.5 mol/L
$R_s/\Omega{\cdot}cm^2$	11.21 ± 2.37	10.54 ± 3.16	10.00 ± 4.38	3.81 ± 5.21
$Q_{f1}/\Omega^{-1}{\cdot}cm^{-2}{\cdot}s^n$	5.97×10^{-5}	5.84×10^{-5}	7.24×10^{-5}	8.34×10^{-5}
n_1	0.91 ± 0.01	0.90 ± 0.01	0.90 ± 0.01	0.89 ± 0.02
$R_{f1}/\Omega{\cdot}cm^2$	10.99 ± 1.35	12.85 ± 2.48	15.67 ± 3.11	6.75 ± 4.26
$Q_{f2}/\Omega^{-1}{\cdot}cm^{-2}{\cdot}s^n$	$4.02 \pm 0.03 \times 10^{-5}$	$2.70 \pm 0.09 \times 10^{-5}$	$1.41 \pm 0.19 \times 10^{-5}$	$2.36 \pm 0.25 \times 10^{-5}$
n_2	0.87 ± 0.02	0.88 ± 0.01	0.96 ± 0.02	0.92 ± 0.01
$R_{f2}/\Omega{\cdot}cm^2$	$4.61 \pm 0.12 \times 10^4$	$1.83 \pm 0.36 \times 10^4$	$1.26 \pm 0.29 \times 10^4$	$0.39 \pm 0.18 \times 10^4$
$W/\Omega{\cdot}cm^2{\cdot}s^{0.5}$	$2.23 \pm 0.21 \times 10^{-4}$	$4.03 \pm 0.42 \times 10^{-4}$	$4.14 \pm 0.29 \times 10^{-4}$	$0.13 \pm 0.08 \times 10^{-4}$
D_O/nm	0.85 ± 0.11	1.39 ± 0.24	1.99 ± 0.04	1.47 ± 0.13

3.4. Potentiodynamic Polarisation

Figure 6 shows the potentiodynamic polarisation curves of the Co-6Ti-11V-9Cr alloy in the four acidic chloride solutions. The alloy exhibited a broad passive region in all media. However, the corrosion potential (E_{corr}), corrosion current density (i_{corr}) and passive current density (i_p) varied markedly with the NaCl concentration. In 0.05 mol/L H_2SO_4 without added NaCl, the alloy showed the highest corrosion potential and a relatively low corrosion current density, indicating the lowest corrosion tendency and slowest corrosion rate. As chloride concentration increased, E_{corr} shifted negatively and i_{corr} increased, indicating a greater susceptibility to corrosion. The electrochemical parameters were obtained by Tafel fitting. At approximately 0.8 V vs. SCE, the anodic current increases continuously, which is attributed to pitting breakdown of the Cr-rich passive film [28,29]. The pitting potential E_{pitt} can be extracted from potentiodynamic curves and presented in Table. 3. Moreover, SEM observations (Figure 7) confirm the occurrence of localised damage on corroded surfaces. With increasing Cl^- concentration, the passive region becomes narrower, indicating that Cl^- deteriorates the stability of passive film and promotes metastable localised corrosion.

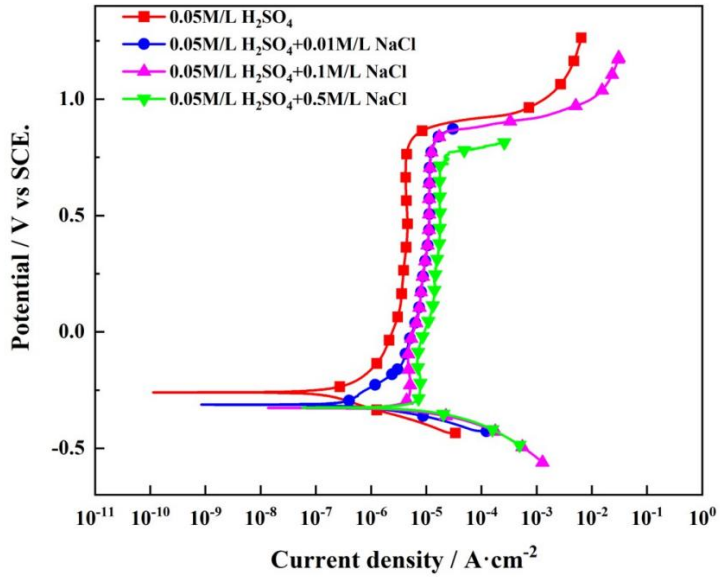


Figure 6. Potentiodynamic polarisation curves of the Co-6Ti-11V-9Cr alloy in the four acidic chloride solutions.

The fitted values of E_{corr}, i_{corr} and i_p are listed in Table 3. E_{corr} decreased overall with an increasing NaCl concentration, indicating reduced thermodynamic stability and lower corrosion resistance. The i_{corr} value measured in 0.01 mol/L NaCl was lower than that in the chloride-free solution, suggesting competition between film formation and film dissolution at low chloride concentration, or a difference that should be interpreted together with replicate-test uncertainty. The passive current density increased with chloride concentration. Because a higher i_p corresponds to faster passive-film dissolution, this trend indicates that chloride ions accelerated passive-film degradation. The polarisation results therefore support the EIS finding that corrosion resistance declined as the NaCl concentration increased.

Table 3. Electrochemical parameters of the Co-6Ti-11V-9Cr alloy in the four acidic chloride solutions.

NaCl Concentration	E_{corr}/V vs. SCE	i_{corr}/A·cm^{-2}	i_p/A·cm^{-2}	E_{pitt}/V vs. SCE
0 mol/L	-0.26 ± 0.01	$5.20 \pm 0.13 \times 10^{-7}$	$4.58 \pm 0.11 \times 10^{-6}$	-0.82 ± 0.06
0.01 mol/L	-0.31 ± 0.02	$4.34 \pm 0.20 \times 10^{-7}$	$1.05 \pm 0.04 \times 10^{-5}$	-0.81 ± 0.05
0.1 mol/L	-0.32 ± 0.01	$2.75 \pm 0.08 \times 10^{-6}$	$1.14 \pm 0.09 \times 10^{-5}$	-0.82 ± 0.02
0.5 mol/L	-0.35 ± 0.03	9.37 ± 0.0610^{-6}	$1.78 \pm 0.08 \times 10^{-5}$	-0.73 ± 0.11

3.5. Corrosion Morphology

Figure 7 shows the corrosion morphologies of the Co-6Ti-11V-9Cr alloy after polarisation in the four acidic chloride solutions. At low NaCl concentrations (0 and 0.01 mol/L), the surface mainly exhibited relatively uniform corrosion. The high-magnification images in Figure 7b,d show clear γ/γ' and Co_3V regions, with only slight dissolution along phase boundaries. This behaviour indicates that the passive film retained a protective effect and partly suppressed matrix dissolution. When the NaCl concentration was increased to 0.1 and 0.5 mol/L, typical corrosion pits appeared on the surface (Figure 7e,g). This localised attack can be attributed to chloride adsorption and dissolution at weak sites or defects in the passive film. It may also be promoted by dissolution near phase boundaries and electrochemical heterogeneity around secondary phases [30]. Overall, increasing the chloride concentration damaged the passive film, enhanced localised corrosion and reduced corrosion resistance, in agreement with the polarisation results.

3.6. Anodic and Cathodic Reactions

In the acidic electrolytes used in this work, the anticipated cathodic partial reactions are hydrogen evolution as the dominant cathodic process, with a minor contribution from the reduction of dissolved oxygen:

$$2H^+ + 2e^- \rightarrow H_2 \quad (4)$$

$$O_2 + 4H^+ + 4e^- \rightarrow 2H_2O \quad (5)$$

The dominance of hydrogen evolution at acidic pH is consistent with previous electrochemical studies on Co–Cr-based alloys in acidic media, in which the anodic dissolution proceeds with the formation of aqueous Co(II) and Cr(II)/Cr(III) species, while the hydrogen evolution reaction dominates the cathodic partial reactions [31,32]. The corresponding anodic dissolution of the alloy can therefore be expressed as

$$Co \rightarrow Co^{2+} + 2e^- \quad (6)$$

$$Cr \rightarrow Cr^{3+} + 3e^- \quad (7)$$

The initial formation of Cr^{2+} and its subsequent oxidation to Cr^{3+} is possible at low pH [29]. The less-noble solutes Ti and V are expected to dissolve in the same manner ($M \rightarrow M^{n+} + ne^-$, M = Ti, V). Simultaneously, Cr and Co are oxidised by water and condense into the bilayer passive film resolved by EIS in Section 3.3 [25,26]:

$$2Cr + 3H_2O \rightarrow Cr_2O_3 + 6H^+ + 6e^- \quad (8)$$

$$Co + H_2O \rightarrow CoO + 2H^+ + 2e^- \quad (9)$$

$$3Co + 4H_2O \rightarrow Co_3O_4 + 8H^+ + 8e^- \quad (10)$$

In the chloride-free acid, film growth (Equations (8)–(10)) and film dissolution (Equations (11) and (12)) nearly balance at relatively noble potentials; the compact Cr_2O_3-rich inner barrier layer then accounts for the high R_{f2} (Table 2) and the low passive current density (Table 3), and corrosion remains essentially uniform (Figures 6 and 7a,b). The passive film is chemically dissolved by the acidic matrix according to

$$Cr_2O_3 + 6H^+ \rightarrow 2Cr^{3+} + 3H_2O \quad (11)$$

$$CoO + 2H^+ \rightarrow Co^{2+} + H_2O \quad (12)$$

and, in the high-potential part of the polarisation scan (above approximately +0.6 V vs. SCE), transpassive oxidation of Cr(III) to soluble chromate may additionally contribute to film thinning [33]:

$$Cr_2O_3 + 5H_2O \rightarrow 2CrO_4^{2-} + 10H^+ + 6e^- \quad (13)$$

When chloride is present, Cl^- adsorbs competitively with oxygen-containing species at weak sites of the passive film (defects, γ/γ' interfaces and Co_3V/matrix interfaces) and forms soluble metal–chloride complexes, which locally thin or rupture the film and trigger pit initiation [34,35]:

$$Me^{n+} + mCl^- \rightarrow [MeCl_m]^{n-m} \text{ (Me = Co, Cr)} \quad (14)$$

Inside the occluded pit, rapid metal dissolution generates cations that hydrolyse and thereby acidify the pit environment:

$$Cr^{3+} + H_2O \rightleftharpoons CrOH^{2+} + H^+ \quad (15)$$

while Cl^- electromigrates into the pit to preserve electroneutrality; the resulting acidified, chloride-rich occluded chemistry is autocatalytic and sustains stable pit growth [35]. The cathodic reactions (Equations (4) and (5)) are then sustained mainly on the surrounding passive surface, and electrons flow through the alloy from the pit (anode) to the passive surface (cathode).

This mechanism consistently accounts for all experimental observations in this work: (i) the negative shifts of OCP (Figure 3) and E_{corr} (Table 3) with an increasing NaCl concentration reflect the increasingly dominant anodic activation of the surface by adsorbed chloride; (ii) the decrease of R_{f2} and R_p (Table 2) originates from chloride-assisted thinning of the inner barrier layer and complexation of film cations [36,37]; (iii) the rising passive current density i_p (Table 3) reflects the accelerated passive-film dissolution described by Equations (10)–(13); and (iv) the SEM morphologies (Figure 7) capture the kinetic consequence of this sequence—at low Cl^- concentrations most film-breakdown events repassivate, whereas at high Cl^- concentrations repassivation is progressively suppressed

and stable pits dominate, in agreement with the chloride-driven transition from uniform corrosion to localised pitting corrosion.

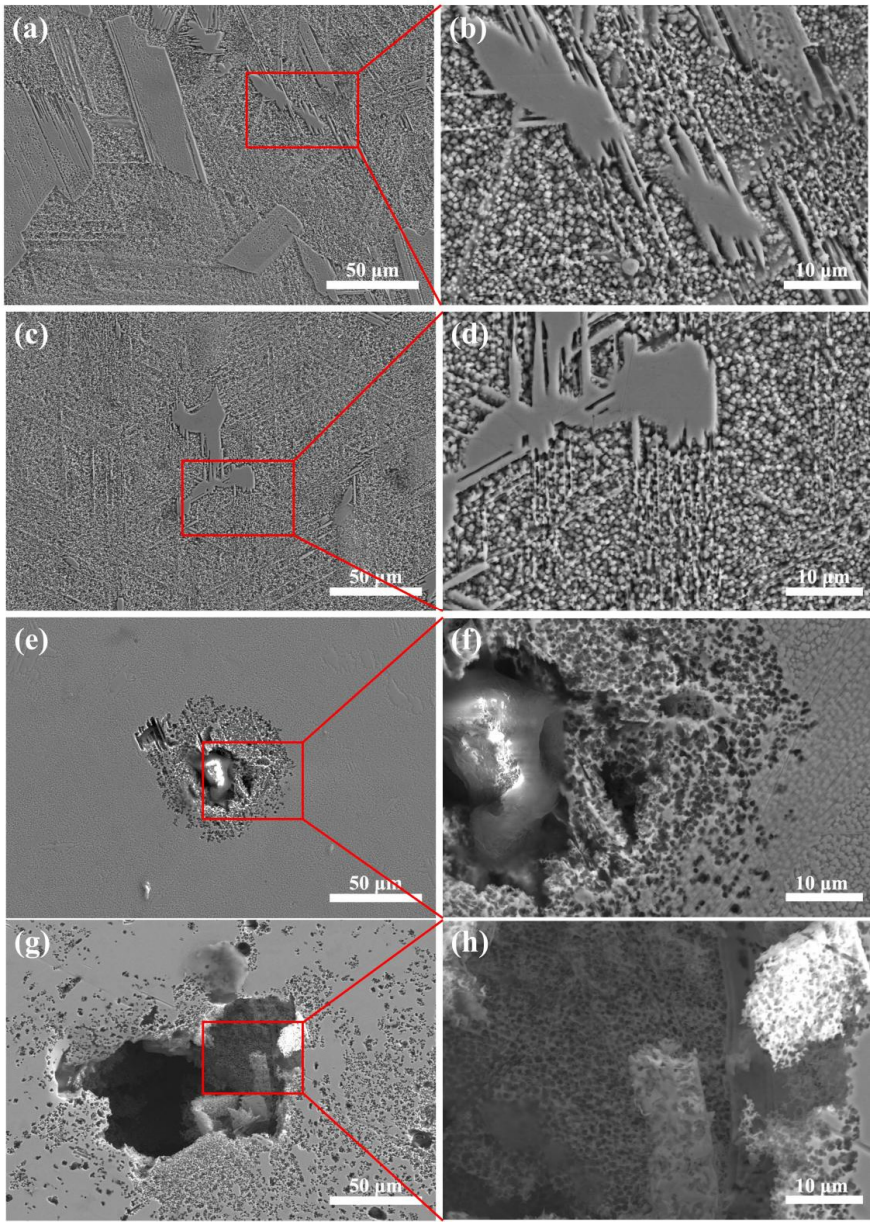


Figure 7. Corrosion morphologies of the Co-6Ti-11V-9Cr alloy after polarisation in the four acidic chloride solutions: (**a**,**b**) 0 mol/L NaCl; (**c**,**d**) 0.01 mol/L NaCl; (**e**,**f**) 0.1 mol/L NaCl; (**g**,**h**) 0.5 mol/L NaCl.

It should be noted that the corrosion products and passive-film constituents suggested in this study, including Cr_2O_3, CoO and Co_3O_4, are inferred based on previous investigations on Co-Cr-based alloys rather than directly identified in the present work. No EDS, XRD, or XPS measurements were performed to experimentally verify the corrosion products formed on the alloy surface after immersion in an acidic chloride-containing solution. Therefore, the exact phases and chemical states of the corrosion products and passive film remain unconfirmed. Further surface-analytical characterisations, such as XPS for element chemical states, XRD for phase identification, and EDS mapping for elemental distribution, are required in future research to provide direct experimental evidence and to fully understand the corrosion mechanism of the Co-6Ti-11V-9Cr superalloy.

4. Electrochemical Noise Analysis

4.1. Transient Analysis

Figure 8 shows the electrochemical potential noise (EPN) and electrochemical current noise (ECN) signals of the Co-6Ti-11V-9Cr alloy in the four acidic chloride solutions. After detrending, the raw noise signals were used to assess the corrosion state of the specimen surface. At low NaCl concentrations, large fluctuations appeared during the early immersion stage (approximately 1 h), indicating local passive-film breakdown followed by repassivation. As the NaCl concentration increased, the amplitudes and peak intensities of both EPN and ECN signals increased, showing enhanced surface activity and a stronger tendency towards localised corrosion.

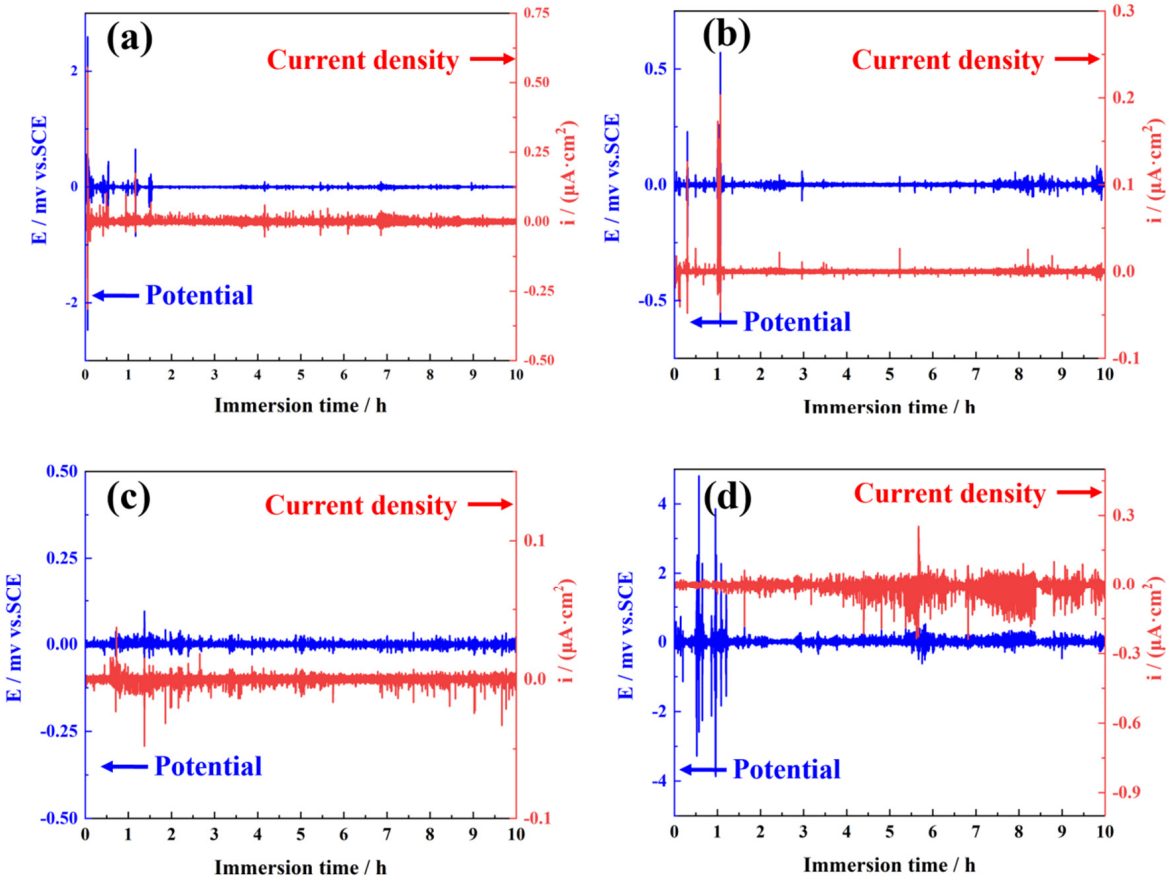


Figure 8. Electrochemical potential noise (EPN) and electrochemical current noise (ECN) signals of the Co-6Ti-11V-9Cr alloy in the four acidic chloride solutions: (**a**) 0 mol/L NaCl; (**b**) 0.01 mol/L NaCl; (**c**) 0.1 mol/L NaCl; (**d**) 0.5 mol/L NaCl.

4.2. Wavelet Analysis

Figure 9 presents the energy distribution plots (EDPs) of current noise for the Co-6Ti-11V-9Cr alloy in the four acidic chloride solutions. In corrosion analysis, the d_1–d_3, d_3–d_6 and d_6–d_8 energy regions are commonly associated with pit initiation/repassivation, metastable pit growth and stable pit growth, respectively [38,39]. In 0.05 mol/L H_2SO_4, the relative energy was mainly concentrated in d_1–d_3, with a small contribution from d_6–d_8. This indicates local passive-film breakdown accompanied by limited local corrosion. When the NaCl concentration increased to 0.01 and 0.1 mol/L, more energy was distributed in d_6–d_8, indicating enhanced localised corrosion. At 0.5 mol/L NaCl, the energy contribution from d_1–d_3 became very small, suggesting sustained passive-film dissolution and stable pit growth.

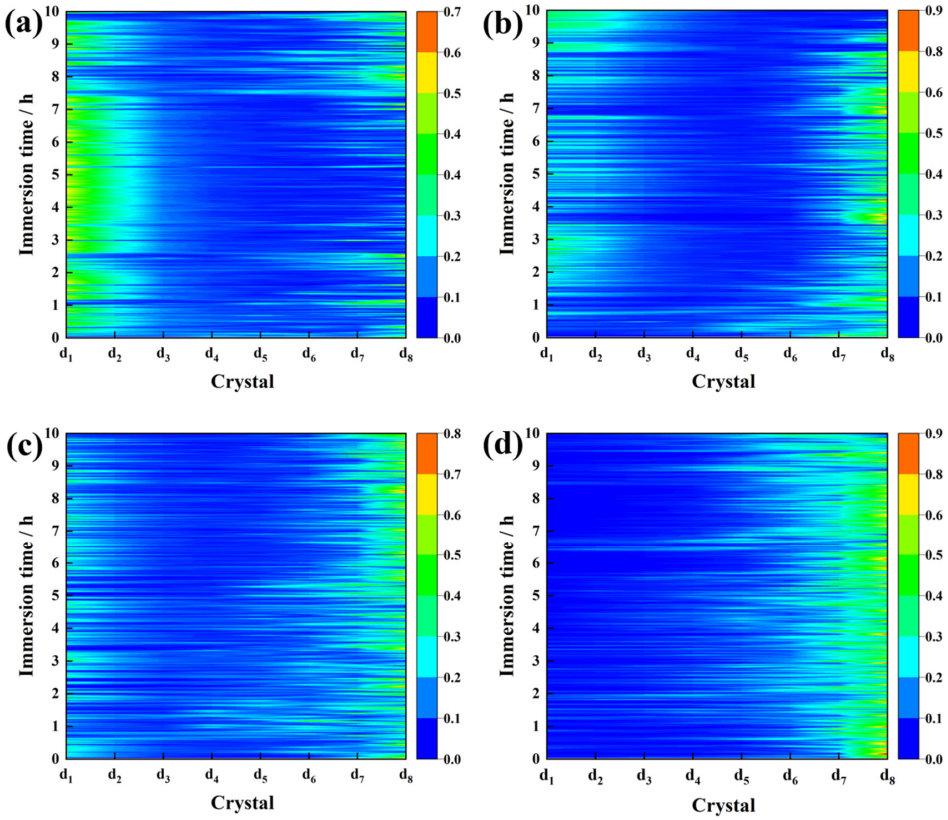


Figure 9. Relative energy distribution of current noise for the Co-6Ti-11V-9Cr alloy in the four acidic chloride solutions: (**a**) 0 mol/L NaCl; (**b**) 0.01 mol/L NaCl; (**c**) 0.1 mol/L NaCl; (**d**) 0.5 mol/L NaCl.

4.3. Shot-Noise Analysis

Figure 10 shows the corrosion characteristic parameters of the Co-6Ti-11V-9Cr alloy in the four acidic chloride solutions. The frequency of corrosion events (f_n) and the charge per corrosion event (q) were used to evaluate the evolution of corrosion mode. A higher f_n indicates a tendency towards more spatially distributed corrosion events, whereas a lower f_n suggests stronger localised corrosion. The value of q reflects the charge released by a single corrosion event. A larger q indicates that localised corrosion is more dominant, whereas a smaller q is more consistent with uniform corrosion. In 0.05 mol/L H_2SO_4, the alloy showed a relatively high f_n and low q, indicating a tendency towards uniform corrosion. As the NaCl concentration increased, f_n decreased and q increased, showing that the surface became more susceptible to pitting. This trend is consistent with local passive-film dissolution.

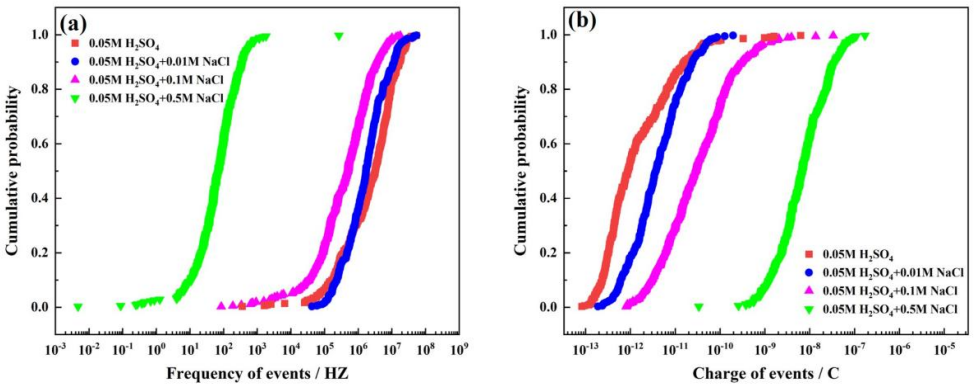


Figure 10. Cumulative distributions of (**a**) fn and (**b**) q for the Co-6Ti-11V-9Cr alloy in the four acidic chloride solutions.

5. Conclusions

The corrosion behaviour of the Co-6Ti-11V-9Cr superalloy in four acidic chloride solutions was investigated using electrochemical measurements, SEM corrosion-morphology observations and EN analysis. The main conclusions are as follows:

(1) The higher chloride concentration reduced the stability of the passive state and increased the corrosion tendency.

(2) EIS results showed that the alloy exhibited passive-film-controlled impedance behaviour in all four solutions. With an increasing NaCl concentration, both the barrier-layer resistance R_{f2} and the polarisation resistance R_p decreased markedly, indicating that chloride ions weakened the barrier effect of the passive film and reduced corrosion resistance.

(3) Potentiodynamic polarisation showed a broad passive region in all solutions. As the NaCl concentration increased, the passive current density ip rose from 4.58×10^{-6} to 1.78×10^{-5} A cm^{-2}, indicating accelerated passive-film dissolution and a faster corrosion process at higher chloride concentration.

(4) Electrochemical noise analysis further revealed the chloride-driven evolution of corrosion modes. Increasing the chloride concentration enlarged the amplitude of potential and current noise transients, and shifted wavelet energy distribution toward stable pit-growth regions. The shot-noise parameters showed a decrease in corrosion-event frequency and an increase in single-event charge, demonstrating the transition from uniform/metastable pitting to stable localised pitting corrosion at higher chloride levels.

It should be noted that all tests in this work were performed in H_2SO_4-containing acidic media. Further investigations on this alloy using various NaCl concentrations without sulphuric acid would help distinguish the individual roles of H^+, SO_4^{2-} and Cl^-, which deserve to be explored in future studies.

Author Contributions: Conceptualisation, P.C., W.L., A.K. and X.Z.; methodology, A.K., W.L. and T.C.; Investigation, P.C., P.Z., W.L., A.K., B.G. and T.C.; writing—original draft preparation, A.K., P.Z., W.L., T.C., B.G. and X.Z.; writing—review and editing, P.Z., T.C., B.G. and X.Z.; supervision, X.Z.; funding acquisition, P.C. All authors have read and agreed to the published version of the manuscript.

Funding: This research was funded with the support by Hydrogen Embrittlement Prevention Technology for Boiler 1's Waterwall (Grant number: ZHP-PY-220041, ZHP-PX-220061, and ZHP-PJ-230030).

Data Availability Statement: The original contributions presented in this study are included in the article. Further inquiries can be directed to the corresponding author.

Conflicts of Interest: Author Peilin Chen, Wenhua Li, Anpeng Kewere, and Bujun Ge were employed by the Guangzhu Electric Power Co., Ltd. of Zhuhai SEZ., and Pengjie Zhang was employed by Luoyang Shuangrui Wanji Titanium Industry Co., Ltd. The remaining authors declare that the research was conducted in the absence of any commercial or financial relationships that could be construed as a potential conflict of interest.

References

1. Chen, L.Y.; Liang, S.X.; Liu, Y.; Zhang, L.-C. Additive manufacturing of metallic lattice structures: Unconstrained design, accurate fabrication, fascinated performances, and challenges. *Mater. Sci. Eng. R Rep.* **2021**, *146*, 100648. [CrossRef]
2. Kaliaraj, G.S.; Siva, T.; Ramadoss, A. Surface functionalized bioceramics coated on metallic implants for biomedical and anticorrosion performance: A review. *J. Mater. Chem. B* **2021**, *9*, 9433–9460. [CrossRef] [PubMed]
3. Li, H.; Shao, S.; Ren, X.; Guo, H.; Lou, D.; Xia, W.; Fang, X. Grain boundary character distribution in the CoCrMo alloy processed by selective laser melting and post-heat treatment. *J. Mater. Sci.* **2020**, *55*, 16780–16790. [CrossRef]
4. Persdotter, A.; Boll, T.; Jonsson, T. Minor element effect on high temperature corrosion of a low-alloyed steel: Insight into alkali- and chlorine induced corrosion by means of atom probe tomography. *Corros. Sci.* **2021**, *192*, 109779. [CrossRef]
5. Klein, L.; Killian, M.S.; Virtanen, S. The effect of nickel and silicon addition on some oxidation properties of novel Co-based high temperature alloys. *Corros. Sci.* **2013**, *69*, 43–49. [CrossRef]

6. Pollock, T.M.; Tin, S. Nickel-based superalloys for advanced turbine engines: Chemistry, microstructure and properties. *J. Propuls. Power* **2006**, *22*, 361–374. [CrossRef]
7. Kracke, A. Superalloys, the most successful alloy system of modern times: Past, present and future. In *Proceedings of the 7th International Symposium on Superalloy 718 and Derivatives, 2010*; John Wiley & Sons, Inc.: Boston, MA, USA, 2010; pp. 13–50.
8. Smith, G.D. Corrosion resistance of nickel-containing alloys in petrochemical environments. In Proceedings of the CORROSION 1997, New Orleans, LA, USA, 9–14 March 1997.
9. Leong, A.; Zhang, J.; Rountree, S.D. Kinetics of corrosion and oxidation of Fe- and Ni-based alloys by molten fluoride salt. *High Temp. Corros. Mater.* **2023**, *99*, 375–397. [CrossRef]
10. Chuvaree, S.; Mookam, N.; Jamkamon, K. An investigation on TIG hardfacing of cobalt-based alloys on tool steels using desirability function. *Arab. J. Sci. Eng.* **2025**, *51*, 17155–17179. [CrossRef]
11. Yu, Q.; Zhang, W.; Shang, J.; Liu, B.; Pei, Y.; Li, Y.; Ao, S. Comparative investigation on the microstructure and corrosion properties of surfacing cobalt alloys by various methods. *Surf. Coat. Technol.* **2024**, *494*, 131386. [CrossRef]
12. Eliaz, N.; Shemesh, G.; Latanision, R.M. Hot corrosion in gas turbine components. *Eng. Fail. Anal.* **2002**, *9*, 31–43. [CrossRef]
13. Sato, J.; Omori, T.; Oikawa, K.; Ohnuma, I.; Kainuma, R.; Ishida, K. Cobalt-base high-temperature alloys. *Science* **2006**, *312*, 90–91. [CrossRef] [PubMed]
14. Yao, Q.; Xing, H.; Sun, J. Structural stability and elastic property of the L12 ordered Co_3(Al,W) precipitate. *Appl. Phys. Lett.* **2006**, *89*, 161906. [CrossRef]
15. Miura, S.; Ohkubo, K.; Mohri, T. Mechanical properties of Co-based L_{12} intermetallic compound Co_3(Al,W). *Mater. Trans.* **2007**, *48*, 2403–2408. [CrossRef]
16. Tanaka, K.; Ohashi, T.; Kishida, K.; Inui, H. Single-crystal elastic constants of Co_3(Al,W) with the L12 structure. *Appl. Phys. Lett.* **2007**, *91*, 181907. [CrossRef]
17. Wang, Y.J.; Wang, C.Y. A comparison of the ideal strength between $L1_2$ Co_3(Al,W) and Ni_3Al under tension and shear from first-principles calculations. *Appl. Phys. Lett.* **2009**, *94*, 261909. [CrossRef]
18. Bocchini, P.J.; Sudbrack, C.K.; Noebe, R.D.; Dunand, D.C.; Seidman, D.N. Effects of titanium substitutions for aluminum and tungsten in Co-10Ni-9Al-9W (at%) superalloys. *Mater. Sci. Eng. A* **2017**, *705*, 122–132. [CrossRef]
19. Makineni, S.K.; Nithin, B.; Chattopadhyay, K. A new tungsten-free γ-γ′ Co-Al-Mo-Nb-based superalloy. *Scr. Mater.* **2015**, *98*, 36–39. [CrossRef]
20. Liu, Y.; Takasugi, T.; Izumi, O. Alloying behavior of Co_3Ti. *Metall. Trans. A* **1986**, *17A*, 1433–1439. [CrossRef]
21. Ruan, J.J.; Liu, X.J.; Yang, S.Y.; Xu, W.; Omori, T.; Yang, T.; Deng, B.; Jiang, H.; Wang, C.; Kainuma, R.; et al. Novel Co-Ti-V-base superalloys reinforced by L12-ordered γ′ phase. *Intermetallics* **2018**, *92*, 126–132. [CrossRef]
22. Li, Y.; Pyczak, F.; Oehring, M.; Wang, L.; Paul, J.; Lorenz, U.; Yao, Z. Thermal stability of γ′ phase in long-term aged Co-Al-W alloys. *J. Alloys Compd.* **2017**, *729*, 266–276. [CrossRef]
23. Karpstein, N.; Laplanche, G.; Saksena, A.; Zehl, R.; Bezold, A.; Horst, O.M.; Bürger, D.; Kostka, A.; Zenk, C.H.; Neumeier, S.; et al. Microscopic mechanism of the L12-D019 phase transformation in a Co-base single crystal superalloy. *Acta Mater.* **2025**, *282*, 120416. [CrossRef]
24. Zhang, P.J.; Ma, L.; Zhou, P.J.; Yang, L.-L.; Emori, W.; Qiao, Y.-X.; Zhang, Q.-C.; Jiang, Y.-S. Cavitation erosion-corrosion behavior of Co–6Ti–11V–9Cr superalloy in 3.5% NaCl solution. *J. Iron Steel Res. Int.* **2025**, *32*, 4440–4453. [CrossRef]
25. Picas, J.A.; Punset, M.; Rupére, E.; Menargues, S.; Martin, E.; Baile, M. Corrosion mechanism of HVOF thermal sprayed WC-CoCr coatings in acidic chloride media. *Surf. Coat. Technol.* **2019**, *371*, 378–388. [CrossRef]
26. Milošev, I.; Strehblow, H.H. The composition of the surface passive film formed on CoCrMo alloy in simulated physiological solution. *Electrochim. Acta* **2003**, *48*, 2767–2774. [CrossRef]
27. Kong, D.; Ni, X.; Dong, C.; Zhang, L.; Yao, J.; Man, C.; Wang, L.; Xiao, K.; Li, X. Anisotropic response in mechanical and corrosion properties of Hastelloy X fabricated by selective laser melting. *Constr. Build. Mater.* **2019**, *221*, 720–729. [CrossRef]
28. Wang, K.; Lan, A.D.; Qiao, J.W. Corrosion behavior of Al0.1CoCrFeNi high entropy alloy in various chloride-containing solutions. *Front. Mater.* **2021**, *7*, 533843. [CrossRef]
29. Qiao, Y.; Zhang, W.; AlMasoud, N.; Shen, X.; Zheng, S.; Alomar, T.S.; El-Bahy, Z.M.; Ibrahim, M.M.; Algadi, H.; Liu, W. Improved passivation and anticorrosion behaviors of selective laser melted Inconel 718 alloy in acidic solutions. *Adv. Compos. Hybrid. Mater.* **2023**, *6*, 204. [CrossRef]
30. Luo, S.; Huang, W.; Yang, H.; Yang, J.; Wang, Z.; Zeng, X. Microstructural evolution and corrosion behaviors of Inconel 718 alloy produced by selective laser melting following different heat treatments. *Addit. Manuf.* **2019**, *30*, 100875. [CrossRef]
31. Contu, F.; Elsener, B.; Böhni, H. Corrosion behaviour of CoCrMo implant alloy during fretting in bovine serum. *Corros. Sci.* **2005**, *47*, 1863–1875. [CrossRef]
32. Benea, L.; Ponthiaux, P.; Wenger, F.; Galland, J.; Hertz, D.; Malo, J.Y. Tribocorrosion of stellite 6 in sulphuric acid medium: Electrochemical behaviour and wear. *Wear* **2004**, *256*, 948–953. [CrossRef]

33. Hodgson, A.W.E.; Kurz, S.; Virtanen, S.; Fervel, V.; Olsson, C.O.A.; Mischler, S. Passive and transpassive behaviour of CoCrMo in simulated biological solutions. *Electrochim. Acta* **2004**, *49*, 2167–2178. [CrossRef]
34. Sato, N. Anodic breakdown of passive films on metals. *J. Electrochem. Soc.* **1982**, *129*, 255–260. [CrossRef]
35. Frankel, G.S. Pitting corrosion of metals: A review of the critical factors. *J. Electrochem. Soc.* **1998**, *145*, 2186. [CrossRef]
36. Zhou, H.L.; Zhu, H.J.; Yang, K.; Zhang, L.M.; Lu, S.; Qiao, Y.X. Carbon-triggered grain boundary engineering in CoCrFeMnNi HEAs: Decoupling the role of M_7C_3 precipitates on passive film stability and localized corrosion resistance. *Int. J. Miner. Metall. Mater.* **2026**. Available online: http://ijmmm.ustb.edu.cn/article/doi/10.1007/s12613-026-3372-2 (accessed on 13 September 2026).
37. Zheng, Z.B.; Liao, X.Y.; Sun, X.; Long, J.; Wang, S.; Qiao, Y.X.; Zheng, K.H. Tailoring reversed austenite and carbide precipitation via tempering to achieve superior impact toughness in high chromium martensitic steels. *J. Iron Steel Res. Int.* **2026**, *33*, 137. [CrossRef]
38. Bahrami, M.J.; Shahidi, M.; Hosseini, S.M.A. Comparison of electrochemical current noise signals arising from symmetrical and asymmetrical electrodes made of Al alloys at different pH values using statistical and wavelet analysis. Part I: Neutral and acidic solutions. *Electrochim. Acta* **2014**, *148*, 127–144. [CrossRef]
39. Xia, D.H.; Song, S.Z.; Behnamian, Y. Detection of corrosion degradation using electrochemical noise (EN): Review of signal processing methods for identifying corrosion forms. *Corros. Eng. Sci. Technol.* **2016**, *51*, 527–544. [CrossRef]

Disclaimer/Publisher's Note: The statements, opinions and data contained in all publications are solely those of the individual author(s) and contributor(s) and not of MDPI and/or the editor(s). MDPI and/or the editor(s) disclaim responsibility for any injury to people or property resulting from any ideas, methods, instructions or products referred to in the content.